

On Inverse Inertia Matrix and Contact-Force Model for Robotic Manipulators at Normal Impacts

Yuquan Wang, Niels Dehio, and Abderrahmane Kheddar

Abstract—We revisit the impact with zero tangential contact velocities caused by an articulated robot arm contacting its rigid environment. The impact behavior depends on the fixed base and multiple rigid links connected by motorized joints. Our thorough analysis focuses on deriving the suitable inverse inertia matrix and a realistic contact-force model. We conducted real-robot experiments with the 7 DOF Panda manipulator, collecting data of 150 impacts with varying joint configurations and different end-effector speeds. Our findings suggest to compute the inverse inertia matrix assuming the joints are locked, i.e., transform the composite-rigid-body inertia at the contact point, and the measurement-consistent contact-force model is viscoelastic.

I. INTRODUCTION

When a robot impacts on rigid surfaces, subsequent impulse forces result in an abrupt change in the robot's joint velocity and torques within a fraction to dozens of milliseconds. If not restricted to their tolerable range, such state jumps may have severe consequences, up to damaging the robot's hardware and surroundings. Therefore, close-to-zero contact velocity is generally planned to avoid impacts [1]. This workaround, however, prevents implementing impact-based tasks like hammering, dynamic loco-manipulations or heavy box swift grabbing to name just a few. A reliable impact model, would allow the robot controller to regulate the velocities relatively to predicted post-impact state jumps.

The state-of-the-art robot controllers [2], [3], [4] predict the impulse by the algebraic equations developed since the late 1980s [5]. Impact studies such in [6], [7], [8], [9] proposed more refined models; yet most of them assumes impacts between two free-flying bodies [10].

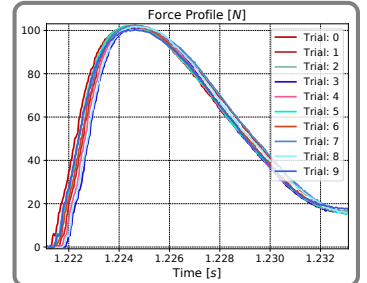
Fixed-base robots under active continuous joint control, cannot bounce freely as assumed in most text-book studied cases, e.g., a bat impacting a ball. In front of the difficulty to have reliable and sound impact predictions using some models tried at an early stage of this study with robots (the Panda robot and the HRP-4 humanoid), we decided to investigate deeply the reasons for this shortcoming. Therefore, we devised a study using the Panda robot in a well-mastered and instrumented environment, e.g., the setup in Fig. 1, and exclude for the time being the humanoid case. Predicting the impact relies on two main ingredients: (i) a reliable *contact-force model* with identifiable parameters, and (ii) a good estimate or the computation of the effective mass i.e., the *inverse inertia matrix* (IIM).

All three authors are with the CNRS-University of Montpellier, LIRMM, Interactive Digital Humans group, Montpellier, France. Email: {yuquan.wang, niels.dehio, kheddar}@lirmm.fr

A. Kheddar is also with the AIST Joint Robotics Laboratory, IRL, Japan.



(a) 7 DOF Panda robot



(b) Contact-force profiles

Figure 1: Applying zero tangential contact velocity, the controller immediately pulls back the end-effector when the collision was detected (in 3-5 ms). The normal contact force are sampled at 25K Hz in Fig. 1(b), where the mean contact velocity is 0.1754 m/s, the mean impact duration is 10.4 ms, and the mean impulse is 0.6662 N·s.

A well-defined IIM [6] allows predicting (a) the post-impact contact mode (i.e., sliding or sticking), (b) the stable slip direction (if the tangential contact velocity converged to an invariant direction), and (c) the contact velocity given an impulse during the impact. We theoretically investigate three possibilities for deriving the IIM based on

- 1) the inverse of the joint-space inertia (classical approach);
- 2) the inverse of the transformed composite-rigid-body (CRB) inertia assuming locked joints;
- 3) concerning the joint flexibilities on top of (b) the idea of treating the robot as a group of rigid bodies connected through bilateral constraints.

Concerning the force measurements from 150 impacts, option (2) provides the most measurement-consistent normal impulse.

Different contact-force models lead to drastically different timing of the events, e.g., *the end of compression* or, more importantly, *the end of restitution*, which determines the impulse and post-impact velocities [8], [9]. Based on the measured contact forces, we found the deformation-rate-dependent (viscoelastic) compliance is not negligible, i.e., the pure elastic contact-force model for two free-flying bodies [8], [7], [11] [6, Chapter 2] is not applicable for multi-body robots. The viscoelasticity enables representing energy-dissipation by damping [12] and indicates a decreasing estimated coefficient of restitution (COR) when the contact velocity increases. In all the experiments, the estimated COR is smaller than the material-dependent COR. Preliminarily, we observed that

when the *locked joints* assumption is approximately valid, i.e., the relative velocity between the center of mass and the contact point is close to zero, and the contact velocity is more significant than 0.1 m/s, the impact is approximately inelastic.

Our analysis is based on the following assumptions:

- The impact force is large compared to body forces and centripetal inertial terms. Other forces remain constant during impact [6, Chapter 8.1.1].
- Point contact. The contact area is negligibly small compared to the robot dimensions [13].
- The impact induces negligible contact moments [6], [13].
- We apply zero tangential velocity (no effects due to friction) in the experiments. The fixed-base robot is fully-actuated and velocity-controlled at 1 ms update rate, which is about one tenth of the average impact duration.
- The impacting bodies in our experiments are locally deformable for the chosen range of contact velocities between 0.08 – 0.18 m/s.

We contribute to the state-of-the-art by:

- I computing IIM by transforming the composite-rigid-body inertia by [14] to the contact point, i.e., the compliance of the impact application point relative to the joint compliance is small [6, Chapter 8.1.1]; see Sec. III,
- II the measurement-consistent contact-force model is viscoelastic, see Sec. IV.
- III the material-dependent COR is not applicable.

II. RELATED WORK

There are three trends to analyze impacts [6], [15], [16]: (a) elastic stress wave propagation; (b) plastic strain theory; and (c) rigid body dynamics. Option (a) can effectively model the energy loss due to vibrations. Option (b) is most applicable to high-velocity impacts, e.g., explosion. In robotics, we do not aim at impacts that generate significant structural deformations. Therefore options (a) and (b) are of limited interest, see [6, Chapter 7,9].

Impact models have also been used in computer graphics animation, see the seminal work in [17]. Yet, in computer graphics what matters is the ‘realism’ of the visual rendering. In robotics, reliable physics simulation is paramount for feeding and assessing planned and controlled impact strategies prior to their implementation on real robotic systems. Therefore, recent investigations benchmark the numerical validity of few well-established models under multiple impacts [18]; whereas a data-driven approach is proposed in [19] to enhance the reliability of the simulation.

The algebraic equations first reported in the late 1980s [5] predict the impulse and the joint velocity jumps based on the kinetic energy conservation. Whereas it does not compute the tangential velocities or impulse. When there is only one tangential velocity direction, i.e., the impact is planar, the post-impact contact mode is limited to re-bounce, sticking, sliding, reverse-sliding. The limited possibilities enable analytical solutions employing Routh’s graphical approach [20] in the impulse space since the early 1990s [21], [22], [23].

When the tangential velocity exists in a plane, i.e., the impact is 3-dimensional, numerical integration is necessary until a specific impact event appears [8]. The impact events include: (1) *sticking*, (2) *stable slip* (the slip direction converges to an invariant line), and (3) *end of restitution* [6]. Employing the IIM, we can predict if sticking can happen and the stable slip direction [6, Eq. 4.12]. Among the available IIM options, i.e., (1) the joint-space IIM [23], [15], (2) the two free-flying body IIM [10], or (3) considering relative velocities between the COM and the contact point [6], we found treating the robot as a composite-rigid body leads to the most measurement-consistent IIM, see Sec. V-E.

The mass-spring-damper system is widely used to model the normal contact force [11]. If the contact material is reasonably soft, e.g., sponge, we can nicely identify the contact-force model and apply a feasible contact velocity [24]. Given that the velocity necessary to initiate yield (deformation) is in the order of 0.1 m/s for structural metals [6, Page 5], e.g., the impact bodies are assumed to be locally deformable. Hence, elasticity is commonly used for impacts between free-flying bodies [6], [8]. However, pure elasticity can not represent energy dissipation, and our measured peak force is not in phase with the compression. Thus, we examined viscoelastic models reported by Stronge [6] to determine the impact events more accurately.

For point contact, there are dozens of continuous contact-force models [25]. However, the model parameters might change over different control modes, and inclusion of contact-force model in the differential equation of motion may result in computational inefficiency or failure of numerical integration routines [23]. Thus, we focus on identifying the model structure, i.e., linear spring and nonlinear dashpot, without explicitly comparing the best-fit model from all the candidates.

III. THE INVERSE INERTIA MATRIX

Assuming impact does not generate impulsive moment, we evaluate the contact velocity $\mathbf{v} \in \mathbb{R}^3$ during the impact via the *inverse inertia matrix* $W \in \mathbb{R}^{3 \times 3}$ and the impulse $\mathbf{\iota} \in \mathbb{R}^3$ [6]:

$$\mathbf{v} = W\mathbf{\iota}.$$

We go through three ways to compute W : (1) inverse of the generalized momentum in Sec. III-A, (2) inverse of the transformed composite-rigid-body (CRB) in Sec. III-B, (3) the CRB approach concerning joint flexibility in Sec. III-C.

We borrowed the notations from the book by Murray *et al.* [26]. To ease the reading, we mark the body velocities and the associated Jacobians by cyan color, e.g., the body velocity of link i concerning the inertial frame \mathcal{F}_O is $\mathbf{V}_{Oi}^b \in \mathbb{R}^6$. We mark the adjoint transform and its expansions by blue color. For instance, the velocity and wrench transform from frame \mathcal{F}_i to the inertial frame \mathcal{F}_O are \mathbf{Ad}_{giO}^{-1} , $\mathbf{Ad}_{giO}^T \in \mathbb{R}^{6 \times 6}$ respectively, where g_{iO} denotes the homogeneous transform from \mathcal{F}_i to \mathcal{F}_O .

A. Projection Approach

Concerning kinetic energy conservation, the body velocity $\mathbf{V}^b \in \mathbb{R}^6$ and the equivalent inertia tensor $I_{eq} \in \mathbb{R}^{6 \times 6}$:

$$\frac{1}{2} \dot{\mathbf{q}}^\top M \dot{\mathbf{q}} = \frac{1}{2} \mathbf{V}^{b\top} \underbrace{(JM^{-1}J^\top)^{-1}}_{I_{eq}} \mathbf{V}^b, \quad (1)$$

computes the same amount of kinetic energy as the joint space inertia tensor $M \in \mathbb{R}^{n \times n}$ and velocities $\dot{\mathbf{q}} \in \mathbb{R}^n$. The equality (1) leads to two options¹:

$$W_{gm} : 3\text{-by-3 upper-left corner of } JM^{-1}J^\top \quad (2)$$

$$m_{em} : 3\text{-by-3 upper-left corner of } (JM^{-1}J^\top)^{-1} \quad (3)$$

The generalized momentum approach [23], [15] employs W_{gm} . Given the (pre-impact) contact velocity $\mathbf{v}^- \in \mathbb{R}^3$ and the coefficient of restitution $e_r \in [0, 1]$, the algebraic equation [5], [2], [3] computes the impulse by (3):

$$\boldsymbol{\iota} = (1 + e_r) m_{em} \mathbf{v}^-. \quad (4)$$

B. Composite-rigid-body approach

Given the external force applied at the contact point \mathbf{p} : $\mathbf{f}_p^b \in \mathbb{R}^3$, the resultant wrench $\mathbf{W}_i^b \in \mathbb{R}^6$ at the i th link writes:

$$\mathbf{W}_i^b = \mathbf{Ad}_{g_{ip}}^\top \begin{bmatrix} \mathbf{f}_p^b \\ 0 \end{bmatrix}. \quad (5)$$

Concerning the mass $m_i \in \mathbb{R}$ and the moment of inertia $\mathcal{I}_i \in \mathbb{R}^{3 \times 3}$, Newton-Euler's equation in the body coordinates writes:

$$\begin{bmatrix} m_i I & 0 \\ 0 & \mathcal{I}_i \end{bmatrix} \begin{bmatrix} \dot{\mathbf{v}}_{O_i}^b \\ \dot{\mathbf{w}}_{O_i}^b \end{bmatrix} + \begin{bmatrix} \mathbf{w}_{O_i}^b \times m_i \mathbf{v}_{O_i}^b \\ \mathbf{w}_{O_i}^b \times \mathcal{I}_i \mathbf{w}_{O_i}^b \end{bmatrix} = \mathbf{W}_i^b. \quad (6)$$

Substituting (5) into (6), we compute the momentum jump $\Delta \mathbf{h}_i$ by integrating (6) over the impact duration δt

$$\Delta \mathbf{h}_i = \begin{bmatrix} m_i I & 0 \\ 0 & \mathcal{I}_i \end{bmatrix} \begin{bmatrix} \Delta \mathbf{v}_{O_i}^b \\ \Delta \mathbf{w}_{O_i}^b \end{bmatrix} = \mathbf{Ad}_{g_{ip}}^\top \begin{bmatrix} \boldsymbol{\iota} \\ 0 \end{bmatrix}, \quad (7)$$

where the cross product of (6) disappeared as the impact force is large compared to the centripetal inertial terms [6, Chapter 8.1.1]. Transforming $\Delta \mathbf{h}_i$ to the centroidal frame \mathcal{F}_c and aggregating over all the links, the centroidal momentum jump is

$$\Delta \mathbf{h} = \sum_{i=1}^n \mathbf{Ad}_{g_{ci}}^\top \Delta \mathbf{h}_i.$$

Given the CRB inertia ${}^{crb}I \in \mathbb{R}^{6 \times 6}$, the jump of the average velocity [14] defined in the centroidal frame writes:

$$\Delta \mathbf{V}_{Oc}^b = {}^{crb}I^{-1} \Delta \mathbf{h}.$$

Concerning the body velocity transform [26, Proposition 2.15], the contact point velocity $\mathbf{V}_{Op}^b \in \mathbb{R}^6$ relative to the centroidal frame \mathcal{F}_c and the inertial frame \mathcal{F}_O writes

$$\mathbf{V}_{Op}^b = \mathbf{Ad}_{g_{cp}}^{-1} \mathbf{V}_{Oc}^b + \mathbf{V}_{cp}^b. \quad (8)$$

¹We reserve the first 3 rows for translational velocity of the Jacobian $J \in \mathbb{R}^{6 \times n}$. If the notations are in line with the book by Featherstone [27], we need to take the lower-right corner.

The *locked-joint assumption* indicates the relative velocity between the centroidal frame and the contact point is zero $\mathbf{V}_{cp}^b = 0$ such that we can approximate:

$$\mathbf{V}_{Op}^b \approx \mathbf{Ad}_{g_{cp}}^{-1} \mathbf{V}_{Oc}^b. \quad (9)$$

Substituting $\Delta \mathbf{V}_{Oc}^b$ and $\Delta \mathbf{h}_i$, the contact point velocity jump induced by the impulse is:

$$\begin{aligned} \Delta \mathbf{V}_{Op}^b &\approx \mathbf{Ad}_{g_{cp}}^{-1} {}^{crb}I^{-1} \Delta \mathbf{h} \\ &= \mathbf{Ad}_{g_{cp}}^{-1} {}^{crb}I^{-1} \sum_{i=1}^n \mathbf{Ad}_{g_{ci}}^\top \Delta \mathbf{h}_i \\ &= \mathbf{Ad}_{g_{cp}}^{-1} {}^{crb}I^{-1} \sum_{i=1}^n \mathbf{Ad}_{g_{ci}}^\top \mathbf{Ad}_{g_{ip}}^\top \begin{bmatrix} \boldsymbol{\iota} \\ 0 \end{bmatrix} \\ &= \mathbf{Ad}_{g_{cp}}^{-1} {}^{crb}I^{-1} \sum_{i=1}^n \mathbf{Ad}_{g_{cp}}^\top \begin{bmatrix} \boldsymbol{\iota} \\ 0 \end{bmatrix} \\ &= \mathbf{Ad}_{g_{cp}}^{-1} {}^{crb}I^{-1} \mathbf{Ad}_{g_{cp}}^\top \begin{bmatrix} \boldsymbol{\iota} \\ 0 \end{bmatrix}. \end{aligned} \quad (10)$$

Left multiply $\mathbf{Ad}_{g_{pc}}^{-1} {}^{crb}I \mathbf{Ad}_{g_{pc}}^{-1}$ to (10), we can see that the equivalent inertia amounts to the CRB inertia transformed to the contact point p :

$$\underbrace{\mathbf{Ad}_{g_{pc}}^{-1} {}^{crb}I \mathbf{Ad}_{g_{pc}}^{-1}}_{\text{Equivalent inertia}} \Delta \mathbf{V}_{Op}^b = \begin{bmatrix} \boldsymbol{\iota} \\ 0 \end{bmatrix}.$$

Extracting the translational part, we obtain the inverse inertia matrix:

$$\Delta \mathbf{v}_{Op}^b = \underbrace{(\frac{I}{m} - R_{cp}^\top \hat{p}_{cp} \mathcal{I}^{-1} \hat{p}_{cp} R_{cp})}_{W} \boldsymbol{\iota}, \quad (11)$$

where $m \in \mathbb{R}$ denotes the entire robot mass, $\mathcal{I} \in \mathbb{R}^{3 \times 3}$ denotes the CRB moment of inertia, and $\hat{p}_{cp} \in \mathbb{R}^3$ denotes the translation of the contact point in the centroidal frame.

C. Composite-rigid-body approach with joint flexibility

When the compliance in joint space is comparable to the Cartesian space counterpart, we need to account for the internal flexibility [6, Sec. 8.1.1], i.e., the non-zero relative velocity: $\mathbf{V}_{cp}^b \neq 0$. We denote the incremental change of W compared to (11) by

$$\tilde{W} = W + W_{\text{flexibility}}. \quad (12)$$

Concerning the kinematics, we compute \mathbf{V}_{cp}^b as:

$$\mathbf{V}_{cp}^b = \mathbf{V}_{Op}^b - \mathbf{Ad}_{g_{cp}}^{-1} \mathbf{V}_{Oc}^b = \underbrace{(\mathbf{J}_{Op}^b - \mathbf{Ad}_{g_{cp}}^{-1} \mathbf{J}_{Oc}^b)}_{\mathbf{J}_{cp}^b \in \mathbb{R}^{6 \times n}} \dot{\mathbf{q}}. \quad (13)$$

To compute the impulse that induces $\Delta \mathbf{V}_{cp}^b$, we need the joint velocity jump as the intermediate variable. Integrate the equations of motion at the moment of the impact [5], [28], we

obtain $M\Delta\dot{\mathbf{q}} = \mathbf{J}_{\mathcal{O}\mathbf{p}}^b \top \begin{bmatrix} \boldsymbol{\iota} \\ 0 \end{bmatrix}$. Hence, $\Delta\dot{\mathbf{q}}$ writes

$$\Delta\dot{\mathbf{q}} = M^{-1} \mathbf{J}_{\mathcal{O}\mathbf{p}}^b \top \begin{bmatrix} \boldsymbol{\iota} \\ 0 \end{bmatrix}. \quad (14)$$

Substituting (14) into the kinematics:

$$\Delta\mathbf{V}_{\mathcal{C}\mathbf{p}}^b = \mathbf{J}_{\mathcal{C}\mathbf{p}}^b \Delta\dot{\mathbf{q}} = \mathbf{J}_{\mathcal{C}\mathbf{p}}^b M^{-1} \mathbf{J}_{\mathcal{O}\mathbf{p}}^b \top \begin{bmatrix} \boldsymbol{\iota} \\ 0 \end{bmatrix},$$

$W_{\text{flexibility}}$ is the 3-by-3 upper-left corner of $\mathbf{J}_{\mathcal{C}\mathbf{p}}^b M^{-1} \mathbf{J}_{\mathcal{O}\mathbf{p}}^b \top$.

IV. THE CONTACT FORCE MODEL

The nonlinear viscoelastic model in Sec. IV-A can generate the measurement-consistent contact-force profile. It predicts a decreasing COR while the contact velocity increases, see Sec. IV-B. Given the non-zero potential energy at the end of restitution, we have to renew the criteria to be used in a numerical procedure, e.g., [8], [10], to determine if the impact ends, see Sec. IV-C.

A. Contact-force model

Placing a virtual viscoelastic model at \mathbf{p} and denote its length by x , see Fig. 3(c), we choose the local coordinate frame such that the initial normal contact velocity $v_n^- \in \mathbb{R}$ is negative: $\dot{x}_0 = v_n^- < 0$. The normal contact-force $f_n \in \mathbb{R}$ is the derivative of the normal impulse $\iota_n \in \mathbb{R}$:

$$\frac{d}{dt}(\iota_n) = f_n = -kx - c|x|\dot{x} = cx\dot{x} - kx, \quad (15)$$

where the scalars c and k denote the virtual dashpot coefficient and the virtual spring constant, x keeps negative $x < 0$ during the impact, and does not restitution to zero, see Fig. 5 in Sec. V.

B. Coefficient of restitution

Employing the definition of the COR, the velocity when the restitution ends is

$$v_{nr} = -e_r v_n^-. \quad (16)$$

At the end of the restitution, the detached contact results in zero contact force. Equating (15) to zero

$$c\dot{x} = k \Rightarrow v_{nr} = \dot{x} = \frac{k}{c},$$

and substituting the COR from (16), we conclude

$$e_r = -\frac{k}{c} \frac{1}{v_n^-}. \quad (17)$$

Therefore, if $\frac{k}{c}$ is constant, e_r decreases if the pre-impact contact velocity v_n^- increases.

C. Energy consistency

At any instant of the impact process, the sum of the kinetic energy E_k , the spring-stored potential energy

$$E_p = \frac{1}{2} kx^2, \quad (18)$$

and the dashpot dissipated energy

$$E_d = \int -cx\dot{x}dx = \int -cx \frac{d}{dt}(x) \frac{d}{dt}(x)dt = \int -cx\dot{x}^2 dt \quad (19)$$

is always equal to the initial kinetic energy:

$$E_k(t_0) = \frac{1}{2}mv_n^-{}^2 = E_k + E_p + E_d. \quad (20)$$

We can verify (20) by checking its derivative. Given $\dot{E}_p = kx\dot{x}$, $\dot{E}_d = -cx\dot{x}^2$ and $\dot{E}_k = m\dot{x}\ddot{x} = \dot{x}f_n = cx\dot{x}^2 - kx\dot{x}$, we find:

$$\dot{E}_k + \dot{E}_p + \dot{E}_d = 0.$$

At the end of the impact process, the energy loss includes the remaining potential energy E_p and the dissipated energy E_d .

V. THE EXPERIMENTAL RESULTS

We apply zero tangential contact velocity in the benchmark experiments. Hence, we assume negligible tangential impulse. Concerning momentum conservation, we predict the impulse at the end of compression ι_{nc} given the IIM and the contact velocity, see Appendix A. The predicted ι_{nc} is compared to the measurement from the experiment setup in Sec. V-A.

We motivate the candidate viscoelastic contact-force model by showing that the virtual-spring model can not generate the measured contact-force profiles unless the COR is greater than 1 in Sec. V-B. The Maxwell model assumes the same COR regardless of the contact velocities, which contradicts the data, see Sec. V-C. The candidate nonlinear viscoelastic model can generate the measured contact-force profile with the theory-consistent COR, see Sec. V-D. From the comparison in Sec. V-E, we conclude that the proposed IIM computation is the most accurate.

A. Impact experiment setup

We impact the 7 DOF panda robot to an ATI-mini45 force-torque sensor through three distinct configurations, see one in Fig. 1(a), two in 3(a), and three in 3(b). In Fig. 3(d) and Fig. 4(d), we denote them by red, blue, and green, respectively.

We sample the force-torque sensor at 25K Hz, which is high enough to capture the dynamics of low-velocity impacts, see Fig. 2. To guarantee the point contact assumption, we mount a 3D-printed semi-spherical end-effector on the panda robot. We cover the force-torque sensor with a flat surface 3D printed by similar material. Through the dropping experiment, similar to [10], the estimated COR is 0.627.

For each impact configuration, the robot impacts at: 0.08 m/s, 0.10 m/s, 0.12 m/s, 0.15 m/s, 0.18 m/s. To remove the random errors, we repeat each combination for 10 times. Hence, the results include $3 \times 5 \times 10 = 150$ experiments in total, i.e., we obtain each dot in Fig. 3(d), Fig. 4(d), and Fig. 7 from 10 experiments. In Fig. 2, we plot 40 contact-force profiles corresponding to the impact configuration in Fig. 1(a).

Exploiting the joint torque sensors, we detect impacts by

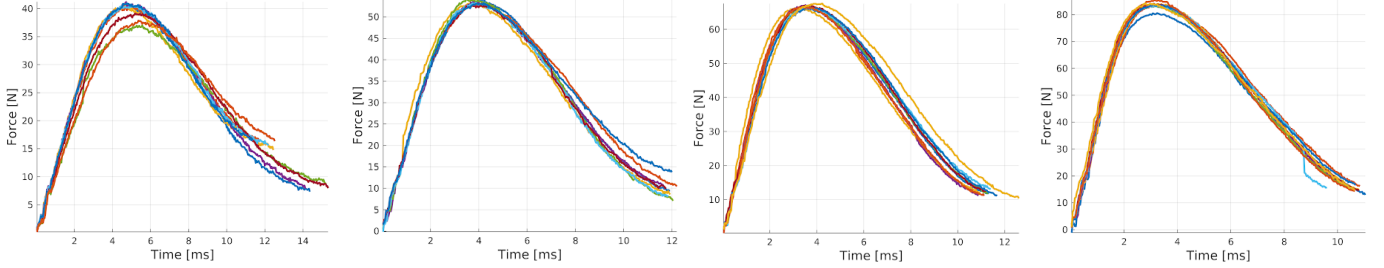


Figure 2: From left to right, we plot four sets of contact-force profiles. Each set includes data from 10 experiments. The corresponding contact velocities are: 0.0755 m/s, 0.0955 m/s, 0.1154 m/s, and 0.1455 m/s. The robot configuration at the impact time is shown in Fig. 1(a). Compared to Fig. 1(b), we do not keep the contact-force profiles corresponding to vibrations after the first fall.

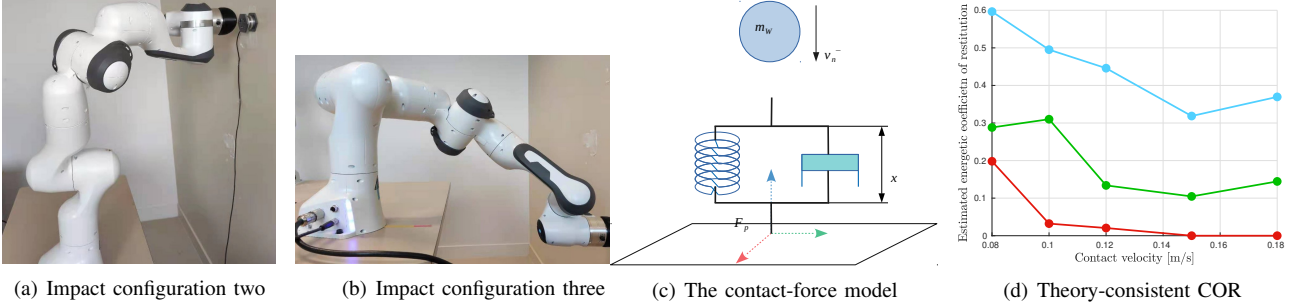


Figure 3: We present two impact configurations in Fig. 3(a) and 3(b). We adopt the parallel connection of a virtual spring and a virtual dashpot model shown in Fig. 3(c) to fit the measured contact-force profiles. For the three impact configurations, the estimated COR in Fig. 3(d) (red, blue, and green for one, two, and three) roughly decreases while the contact velocity increases, which mostly agrees with the analysis in Sec. IV-B and [6, Chapter 5.1.2]. The difference is due to the fact that the spring stiffness and the damper constant vary over different contact velocities.

thresholding the sum of the 5th and 6th joint torque error:

$$\sum_{i=5}^6 |\tau_i - \tau_i^*|.$$

We achieved 3 to 5 ms detection time, which is comparable to the state-of-the-art collision detection time: 3 ms [29].

B. The virtual spring model

Given the schematic view in Fig. 4(a), the contact force and the compression are perfectly in phase, i.e., the maximum contact force is reached when the compression ends. Therefore, if the COR fulfills: $0 < e_r < 1$, the contact-force profile during restitution should be within the blue area in Fig. 4(b), see more details by [6, Chapter 2.2]. For instance, it could cover an area marked by green. However, concerning Fig. 4(b), the virtual-spring model can not generate the measured contact profiles, unless the coefficient of restitution e_r is greater than 1. We can find similar patterns of the contact-force profiles in all the measurements in Fig. 2.

Therefore, we conclude that the contact force shall be out-of-phase with the compression by some angle, i.e., the peak contact-force occurs ahead of the maximum compression, which corresponds to the viscoelasticity.

C. The Maxwell model

We illustrate the Maxwell model (series connection of a virtual spring with stiffness $k \in \mathbb{R}$ and a dashpot with constant $c \in \mathbb{R}$) in Fig. 4(c). The complete linear second-order system is detailed by [6, Chapter 5.1.1]. We fed the measured contact-force profiles to the grey-box estimator in MATLAB to identify k , c , and ultimately the COR according to [6, Eq. 5.7]. The estimated COR should be invariant with respect to the increasing contact velocities. However, in Fig. 4(d), this assumption contradicts the COR estimated from the measurements.

D. The nonlinear viscoelastic model

Following the same procedure in Sec. V-C, we identify the virtual spring coefficient k and the virtual dashpot constant $c \in \mathbb{R}$ for the nonlinear viscoelastic model (15), see the second-order dynamics by [6, Chapter 5.1.2].

We overlay the regenerated contact-force profiles on the validation measurements in Fig. 5. Due to the viscoelasticity, the compression x might not fully restore to zero when the restitution ends. According to (17), the COR decreases while the contact velocity increases. In Fig. 3(d), we can find this is mostly true. The exception happens at the second impact configuration when the reference contact velocity is 0.08 m/s.

The virtual spring model in Fig. 4(a) can not capture the energy dissipation. It entirely relies on the COR to model the

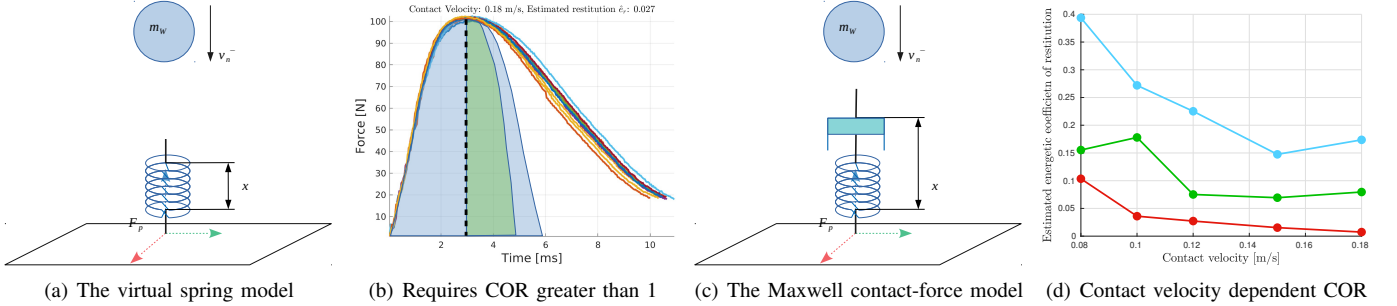


Figure 4: Zooming in the contact-force profiles of Fig. 1(b), we cut the contact-force profiles at about 20 N in Fig. 4(b). The light blue color illustrates the area below the contact-force profile when the coefficient of restitution e_r is 1. The green area is an example when $0 < e_r < 1$. If $e_r = 0$, the contact-force profile finishes along the dashed-black line, where the maximum contact force locates. The COR estimated by the series connection of a virtual spring and a virtual dashpot shown in Fig. 4(c) for three different robot configurations (red, blue, and green for one, two, and three) are shown in Fig. 4(d).

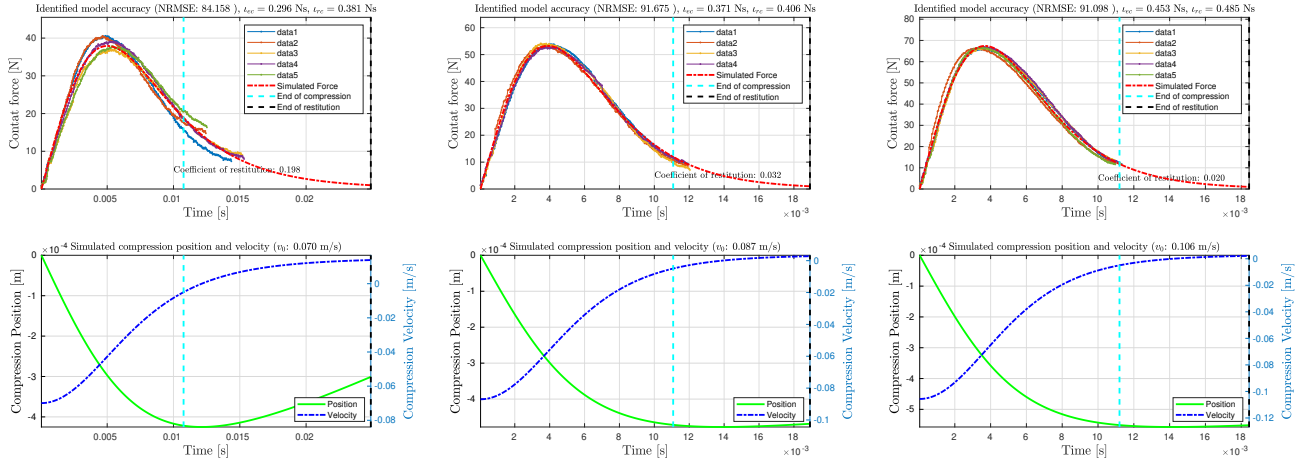


Figure 5: We overlay the contact-force generated from the nonlinear viscoelastic model (15) on the measurements. From left to right, the contact velocities are 0.0755, 0.0955, and 0.1154 m/s. We mark the moments (1) when the compression ends, i.e., the compression rate is zero $\dot{x} = 0$ and (2) the restitution ends, i.e., the contact-force is zero $f_n = 0$. Through the impact process, the \dot{x} increases monotonically from the negative initial value. The compression might not restore to zero.

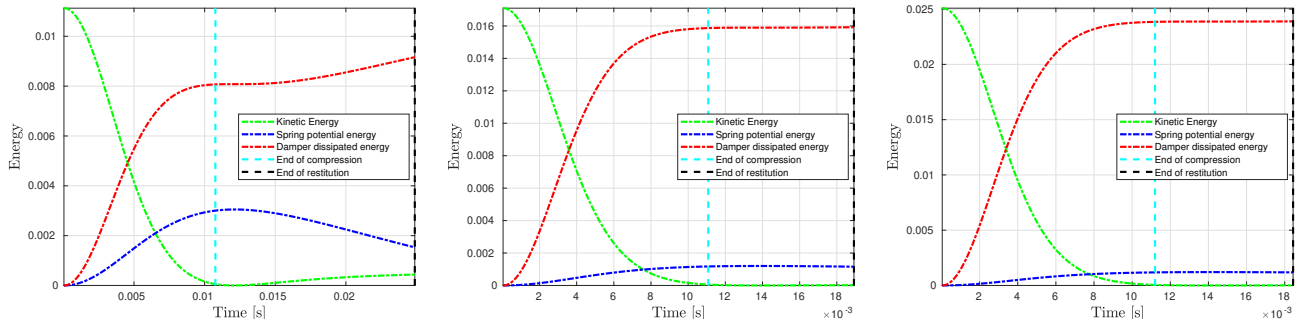
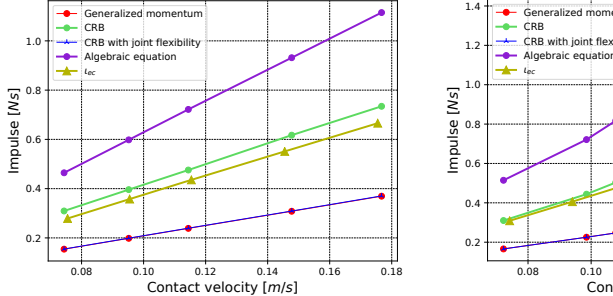
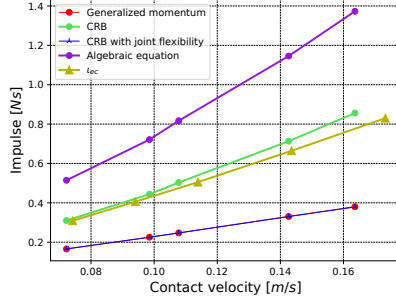


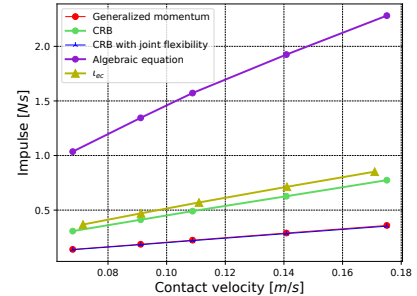
Figure 6: The sum of the potential energy (18), the dissipated energy (19), and the kinetic energy is equal to the initial kinetic energy: $\frac{1}{2}mv_n^{-2}$, see (20).



(a) Impulses corresponding to Fig. 1(a)



(b) Impulses corresponding to Fig. 3(a)



(c) Impulses corresponding to Fig. 3(b)

Figure 7: The ι_{nc} by different IIM candidates against the measurements. Each point is the mean of 10 impact experiments. The CRB approach (11) is close to the measured impulse (the yellow triangles). The algebraic equation (4) overestimates, while the CRB concerning joint flexibilities (12) and the generalized momentum approach (2) underestimate.

energy loss. For instance, there exists a sudden decrease of the potential energy by $e_r^2 \frac{1}{2} m v_n^{-2}$ at the moment when the compression ends [10, Eq. 11, Fig. 3.(h)]. Due to the dashpot, we can explicitly and continuously describe the potential, kinetic, and dissipated energy along with their derivatives; see the equations in Sec. IV-C and the plots in Fig. 6. The following assumptions used in [7], [8] are not applicable for robot impacts: (1) the potential energy E_p reaches the peak at the maximum contact force. (2) the compression restores to zero when the restitution ends.

Hence, the end of the restitution (or the entire impact duration), depends on if the contact force (15) decreases to zero.

Table I. Given the reference \mathbf{V}_{Op}^b , we compare the exact contact velocities by (8), and the approximation by (9).

Reference:	0.08	0.10	0.12	0.15	0.18
Exact \mathbf{V}_{Op}^b by (8).					
Fig. 1(a)	0.0756	0.0956	0.1156	0.1456	0.1755
Fig. 3(a)	0.0745	0.0943	0.1141	0.1438	0.1734
Fig. 3(b)	0.0715	0.0913	0.1111	0.1411	0.1709
Approximation: $\mathbf{V}_{Op}^b - \mathbf{V}_{cp}^b$ by (9).					
Fig. 1(a)	0.0699	0.0870	0.1056	0.1309	0.1623
Fig. 3(a)	0.0567	0.0734	0.0975	0.1239	0.1486
Fig. 3(b)	0.0446	0.0586	0.0712	0.0894	0.1036
Approximate-to-exact ratio: $\frac{\text{Ad}_{gep}^{-1} \mathbf{V}_{Op}^b}{\mathbf{V}_{Op}^b}$.					
Fig. 1(a)	0.9248	0.9100	0.9141	0.8996	0.9243
Fig. 3(a)	0.7609	0.7785	0.8544	0.8618	0.8567
Fig. 3(b)	0.6244	0.6423	0.6406	0.6336	0.6062

E. Candidate inverse inertia matrices

We compare the impulse ι_{nc} when the compression ends against the measurements employing different IIM candidates:

- 1) the algebraic equation (4), see [5], [2], [3], [4],
- 2) the generalized momentum approach (2), see [15], [23].
- 3) the CRB approach (11),
- 4) the CRB with joint flexibility (12), see [6, Sec. 8.1.2].

Concerning Fig. 7, option 1 overestimates in all the cases. Hence, computing Cartesian space momentum according to kinetic energy conservation in joint space (1) is not a reasonable hypothesis. Option 2 and 4 lead to similar results, and both underestimate. Thus, we can not assume the joints are completely flexible such as the under-actuated pendulum by Lankarani [23], and the under-actuated linkage by Stronge [6, Example 8.1].

Transforming the CRB inertia to the contact point and assuming the joints are locked, option 3 leads to the most accurate prediction. Therefore, our intuitive *locked-joint* assumption applies to compute the Cartesian space momentum at a contact point for a high-stiffness-controlled robot.

The relative velocity \mathbf{V}_{cp}^b is the difference between the exact computation (8) and the approximate (9). When the locked-joints assumption is approximately valid, the relative velocity \mathbf{V}_{cp}^b is close to zero, and the approximate-to-exact ratio in $\frac{\text{Ad}_{gep}^{-1} \mathbf{V}_{Op}^b}{\mathbf{V}_{Op}^b}$ in Table I is closer to 1.

Comparing Fig. 3(d), we can assume a COR smaller than 0.1, i.e., approximately inelastic impact, for our experiment setup if the following are met: (1) when \mathbf{V}_{cp}^b is close to zero, and (2) the contact velocity is greater than 0.1 m/s,

VI. CONCLUSION

Our work revisit some ingredients of impact models used in robotics. According to our experimental findings, state-of-the-art robot controllers base on algebraic equations proposed in [5], [2], [3] to compute impact-induced state jumps leads to noticeable errors.

The latest impact dynamics model, e.g., [6], [7], [8], [9], are mostly tailor-made for two-floating-bodies impacts. To exploit them for articulated robots controlled by high-stiffness joint controllers, we examine two essential components:

- the inverse inertia matrix (IIM) that determines (1) the contact mode, (2) the stable sliding direction, and (3) the impulse at different impact events.
- the contact-force model that determines the impact event timing, e.g., if the restitution has finished.

Comparing against the 150 measured contact-force profiles, we conclude that (1) we shall compute the inverse inertia matrix (IIM) as the inverse of the composite-rigid-body inertia transformed at the contact point, see Sec. III-B; (2) the widely-used virtual spring model [7], [8], [15] is deficient for impacts with high-stiffness controlled robots; (3) the viscoelastic contact-force model (parallel connection of a virtual spring and a dashpot) in Sec. IV-A can match the measurements while fulfilling its assumptions.

The proposed IIM and the contact-force model enable integrating the latest impact dynamics model into the robot controller. Employing the improved post-impact state prediction, the robot could exploit high contact velocities while fulfilling the constraints regarding hardware limits.

ACKNOWLEDGEMENT

This work is supported by the Research Project I.AM. through the EU H2020 program under GA 871899. We would like to thank our colleague J. Roux, S. Samadi and O. Tempier for actively helping in the experiments.

REFERENCES

- [1] A. W. Winkler, C. D. Bellicoso, M. Hutter, and J. Buchli, “Gait and trajectory optimization for legged systems through phase-based end-effector parameterization,” *IEEE Robotics and Automation Letters*, vol. 3, no. 3, pp. 1560–1567, 2018.
- [2] J. W. Grizzle, C. Chevallereau, R. W. Sinnet, and A. D. Ames, “Models, feedback control, and open problems of 3d bipedal robotic walking,” *Automatica*, vol. 50, no. 8, pp. 1955–1988, 2014.
- [3] B. Siciliano and O. Khatib, *Springer handbook of robotics*. Springer, 2016.
- [4] I. Aouaj, V. Padois, and A. Saccon, “Predicting the post-impact velocity of a robotic arm via rigid multibody models: an experimental study,” in *IEEE International Conference on Robotics and Automation (ICRA)*, 2021.
- [5] Y.-F. Zheng and H. Hemami, “Mathematical modeling of a robot collision with its environment,” *Journal of Field Robotics*, vol. 2, no. 3, pp. 289–307, 1985.
- [6] W. J. Stronge, *Impact mechanics*. Cambridge university press, 2000.
- [7] Y.-B. Jia, M. T. Mason, and M. A. Erdmann, “Multiple impacts: A state transition diagram approach,” *The International Journal of Robotics Research*, vol. 32, no. 1, pp. 84–114, 2013.
- [8] Y.-B. Jia and F. Wang, “Analysis and computation of two body impact in three dimensions,” *Journal of Computational and Nonlinear Dynamics*, vol. 12, no. 4, p. 041012, 2017.
- [9] M. Halm and M. Posa, “Modeling and analysis of non-unique behaviors in multiple frictional impacts,” 2019.
- [10] Y.-B. Jia, M. Gardner, and X. Mu, “Batting an in-flight object to the target,” *The International Journal of Robotics Research*, vol. 38, no. 4, pp. 451–485, 2019.
- [11] S. Pashah, M. Massenzio, and E. Jacquelin, “Prediction of structural response for low velocity impact,” *International Journal of Impact Engineering*, vol. 35, no. 2, pp. 119–132, 2008.
- [12] H. M. Lankarani and P. E. Nikravesh, “Continuous contact force models for impact analysis in multibody systems,” *Nonlinear Dynamics*, vol. 5, no. 2, pp. 193–207, 1994.
- [13] A. Chatterjee and A. Ruina, “A new algebraic rigid-body collision law based on impulse space considerations,” 1998.
- [14] D. E. Orin and A. Goswami, “Centroidal momentum matrix of a humanoid robot: Structure and properties,” in *IEEE/RSJ International Conference on Intelligent Robots and Systems*, 2008, pp. 653–659.
- [15] Y. Khulief, “Modeling of impact in multibody systems: an overview,” *Journal of Computational and Nonlinear Dynamics*, vol. 8, no. 2, 2013.
- [16] S. Faik and H. Witteman, “Modeling of impact dynamics: A literature survey,” in *2000 International ADAMS User Conference*, vol. 80. Citeseer, 2000.
- [17] B. V. Mirtich, *Impulse-based dynamic simulation of rigid body systems*. University of California, Berkeley, 1996.
- [18] N. S. Nguyen and B. Brogliato, “Comparisons of multiple-impact laws for multibody systems: Moreau’s law, binary impacts, and the lzb approach,” in *Advanced Topics in Nonsmooth Dynamics*. Springer, 2018, pp. 1–45.
- [19] Y. Jiang, J. Sun, and C. K. Liu, “Data-augmented contact model for rigid body simulation,” *arXiv preprint arXiv:1803.04019*, 2018.
- [20] E. J. Routh *et al.*, *Dynamics of a system of rigid bodies*. Dover New York, 1955.
- [21] Y. Wang and M. T. Mason, “Two-dimensional rigid-body collisions with friction,” *Journal of Applied Mechanics*, vol. 59, no. 3, p. 635, 1992.
- [22] Y. Hurmuzlu and D. B. Marghitu, “Rigid body collisions of planar kinematic chains with multiple contact points,” *The international journal of robotics research*, vol. 13, no. 1, pp. 82–92, 1994.
- [23] H. M. Lankarani, “A poisson-based formulation for frictional impact analysis of multibody mechanical systems with open or closed kinematic chains,” *Journal of Mechanical Design*, vol. 122, no. 4, pp. 489–497, 2000.
- [24] N. Dehio and A. Kheddar, “Robot-safe impacts with soft contacts based on learned deformations,” in *IEEE International Conference on Robotics and Automation (ICRA)*, 2021. [Online]. Available: <https://hal.archives-ouvertes.fr/hal-02973947>
- [25] L. Skrinjar, J. Slavič, and M. Boltežar, “A review of continuous contact-force models in multibody dynamics,” *International Journal of Mechanical Sciences*, vol. 145, pp. 171–187, 2018.
- [26] R. M. Murray, Z. Li, S. S. Sastry, and S. S. Sastry, *A mathematical introduction to robotic manipulation*. CRC press, 1994.
- [27] R. Featherstone, *Rigid body dynamics algorithms*. Springer, 2014.
- [28] Y. Wang and A. Kheddar, “Impact-friendly robust control design with task-space quadratic optimization,” in *Proceedings of Robotics: Science and Systems*, vol. 15, Freiburg, Germany, 24–26 June 2019, p. 32.
- [29] S. A. B. Birjandi, J. Kühn, and S. Haddadin, “Observer-extended direct method for collision monitoring in robot manipulators using proprioception and imu sensing,” *IEEE Robotics and Automation Letters*, vol. 5, no. 2, pp. 954–961, 2020.

APPENDIX

A. Post-impact states computation

The impact process consists of two sequential phases: compression and restitution [8]. The compression ends when the normal contact velocity increases from $v_n^- < 0$ to zero. To check the evolution of v_n , we compute its derivative:

$$\frac{dv_n}{dt_n} = \frac{d(v_n^- + \hat{\mathbf{n}}^\top W \boldsymbol{\iota})}{dt_n} = \hat{\mathbf{n}}^\top W \frac{d\boldsymbol{\iota}}{dt_n} = \hat{\mathbf{n}}^\top W \hat{\mathbf{n}} + \hat{\mathbf{n}}^\top W \frac{d\boldsymbol{\iota}_\perp}{dt_n},$$

where the vector $\hat{\mathbf{n}} \in \mathbb{R}^3$ denotes the impact normal, the subscript \perp denotes the quantity is projected to the tangential plane. Due to negligible tangential impulse assumption, we have $\frac{d\boldsymbol{\iota}_\perp}{dt_n} = 0$. The contact velocity v_n monotonically increases according to:

$$\frac{dv_n}{dt_n} = \frac{d(v_n^- + \hat{\mathbf{n}}^\top W \boldsymbol{\iota})}{dt_n} = \hat{\mathbf{n}}^\top W \frac{d\boldsymbol{\iota}}{dt_n} = \hat{\mathbf{n}}^\top W \hat{\mathbf{n}} > 0, \quad (21)$$

which holds due to the positive definiteness of W [10]. Integrating (21) by separating dv_n and $d\boldsymbol{\iota}_n$ on two sides, the impulse is:

$$\boldsymbol{\iota}_n = \mathbf{m}_W(v_n - v_n^-), \quad (22)$$

where we defined the positive scalar $\mathbf{m}_W = \frac{1}{\hat{\mathbf{n}}^\top W \hat{\mathbf{n}}}$. At the moment when $v_n = 0$, we conclude the end-of-compression impulse:

$$\boldsymbol{\iota}_{nc} = -\frac{v_n^-}{\hat{\mathbf{n}}^\top W \hat{\mathbf{n}}} = -\mathbf{m}_W v_n^-. \quad (23)$$